ACCSCIENCE PUBLISHING

Materials Science in Additive Manufacturing

ORIGINAL RESEARCH ARTICLE

Laser-assisted cold spray additive manufacturing of Ti6Al4V: Synergistic evolution of microstructure refinement and interface bonding

Shaowu Liu[1,2]*, Shen Wang[1,2], Yehao Zhang[1,2], Hongjian Wu[3], Wenbo Li[4], Bo Li[1,2], Zexin Yu[1,2], Panpan Zhang[1,2], Shuo Yin[5], Qunli Zhang[1,2], Hanlin Liao[6], and Jianhua Yao[1,2]*

[1]Institute of Laser Advanced Manufacturing, Zhejiang University of Technology, Hangzhou, Zhejiang, China

[2]College of Mechanical Engineering, Zhejiang University of Technology, Hangzhou, Zhejiang, China

[3]Institute of Materials Science, Helmut Schmidt University, Hamburg, Hamburg, Germany

[4]National Engineering Laboratory of Modern Materials Surface Engineering Technology, Guangdong Provincial Key Laboratory of Modern Surface Engineering Technology, Institute of New Materials, Guangdong Academy of Sciences, Guangzhou, Guangdong, China

[5]Department of Mechanical, Manufacturing & Biomedical Engineering, Trinity College Dublin, The University of Dublin, Dublin, Leinster, Ireland

[6]Laboratoire of Interdisciplinary Carnot of Bourgogne (ICB UMR 6303 CNRS), University of Bourgogne-Franche-Comté, Belfort, Bourgogne-Franche-Comté, France

***Corresponding authors:**
Shaowu Liu
(shaowuliu@zjut.edu.cn);
Jianhua Yao
(lam@zjut.edu.cn)

Citation: Liu S, Wang S, Zhang Y, *et al*. Laser-assisted cold spray additive manufacturing of Ti6Al4V: Synergistic evolution of microstructure refinement and interface bonding. *Mater Sci Add Manuf*. 2026;5(3):026220048. doi: 10.36922/MSAM026220048

Received: May 25, 2026

Revised: June 29, 2026

Accepted: July 6, 2026

Published online: July 23, 2026

Abstract

The aluminum/titanium (Al/Ti) couple is a typical "limited mutual solubility heterogeneous metal" system, in which fusion-based manufacturing often leads to brittle intermetallic compounds and cracks. This study systematically investigates the microstructure and mechanical properties of Ti6Al4V deposited on 6061Al substrates via laser-assisted cold spray (LACS). X-ray diffraction (XRD) results confirm that the process maintains solid-state deposition characteristics, with only the α-Ti phase detected, indicating no detectable Al/Ti intermetallic compounds by XRD across all conditions. Laser assistance significantly enhanced deposition layer densification; at 600 W, the porosity decreased from 11.81% to 0.41%. Electron backscatter diffraction and transmission electron microscopy (TEM) characterizations revealed that the LACS process triggered intense dynamic recrystallization, refining the average grain size from 1.906 μm to 0.813 μm. High-resolution TEM analysis further identified a nanoscale grain gradient and a ~5 μm elemental transition zone layer at the bonding interface, demonstrating the formation of a compositionally graded interfacial region accompanied by mechanical interlocking and localized elemental redistribution. Performance tests showed that increasing the laser power increased the microhardness to 388.1 $HV_{0.2}$. Compared to cold spraying, the LACS-600 W samples achieved a 40% increase in ultimate tensile strength (206.58 MPa) and a 100% improvement in elongation (2.17%). The results indicate that LACS provides a high-performance solid-state additive manufacturing solution for Ti6Al4V/6061Al heterogeneous structures through the synergistic effects of laser-induced thermal accumulation and particle tamping densification.

Keywords: Ti6Al4V/6061Al; Laser-assisted cold spray; Solid-state deposition; Dynamic recrystallization; Mechanical properties

1. Introduction

Aluminum/titanium (Al/Ti) composite materials combine the lightweight and high thermal conductivity of Al with the high strength and corrosion resistance of Ti, thereby possessing excellent characteristics such as high specific strength and superior high-temperature performance.[1] Existing studies have pointed out that these composites are widely used in fields with high demand for lightweight and high-performance materials, such as the aerospace and automotive industries, due to their “lightweight, high strength, and good high-temperature performance”.[2] A typical combination involves the joint use of an Al alloy with good workability (e.g., 6061 Al alloy) and a Ti alloy with superior properties (e.g., Ti6Al4V for aerospace structures). 6061 Al alloy offers low density and good thermal conductivity, while Ti6Al4V Ti alloy features high strength and excellent corrosion resistance. Compounding the two can enhance the mechanical strength and durability of components while simultaneously reducing weight, meeting the stringent requirements for comprehensive material performance in modern aerospace, automotive, and other sectors.[3]

However, Al/Ti belongs to a typical “limited mutual solubility heterogeneous metal” system, characterized by significant differences in physical and chemical properties,[4] poor metallurgical compatibility,[5] and high sensitivity to heat input.[6] In high-heat-input fusion additive manufacturing processes, such as laser cladding,[7] selective laser melting,[8] and laser powder bed fusion,[9] brittle intermetallic compounds are easily formed in the heat-affected zone and induce high internal stresses. This leads to prominent issues such as interfacial or interlaminar cracks, residual stress, and deformation during the manufacturing of heterogeneous materials, which often necessitate multiple post-treatments to satisfy service requirements.[10]

Cold spray (CS) is a solid-state metal deposition technology that utilizes heated high-pressure gas (typically nitrogen, helium, or compressed air) to accelerate metal powder to supersonic speeds, which then impacts the substrate to achieve bonding through plastic deformation.[11] Compared with laser cladding, selective laser melting, and laser powder bed fusion, the formation of cold-sprayed deposits depends primarily on the kinetic energy of the particles before impact rather than on thermal energy.[12] It is this low-temperature deposition process that ensures the powder remains in a solid state, avoiding common problems associated with traditional high-temperature processes, such as oxidation, residual stress, and phase transformation, thereby allowing the original physical and chemical properties of the material to be well preserved.[13,14] Consequently, CS demonstrates unique advantages in the deposition of heat-sensitive materials (e.g., amorphous[15] and nanomaterials[16]), oxidation-sensitive materials (e.g., Ti,[17,18] copper,[19,20] and Al[21,22]), and phase-change sensitive materials (e.g., carbon-based reinforced metal matrix composites such as diamond and carbon nanotubes[23,24]).

Regarding the preparation of Al/Ti composites, scholars have explored the application of CS. For example, an Al-core/Ti-skin structure was constructed by layer-by-layer deposition of pure Ti powder on an Al substrate;[25] Drehmann *et al.*[26] applied Ti powder onto 6061-T6 Al alloy substrates via CS and subsequently subjected the coatings to die forging and rotary swaging to improve bonding strength and density. Additionally, research has investigated co-spraying Al and Ti powders to form coatings containing intermetallic compounds, such as $TiAl_3$ on the substrate,[27] aiming to balance the advantages of both phases. However, these studies indicate that controlling the formation of intermetallic phases and optimizing interfacial bonding in the Al/Ti system remain challenging, and the optimization of relevant processes and parameters is actively being pursued.

Laser-assisted cold spray (LACS) is a new deposition technology developed in recent years that combines laser heating with the CS process.[28,29] Its basic principle involves using a laser for in situ local preheating of the substrate and powder particles during the spraying process, creating a transient heating zone on the substrate ahead of the particle impact.[30] This preheating can soften the substrate surface and powder particles, thereby significantly improving interfacial bonding and coating density.[31,32] In other words, laser preheating can reduce the critical deposition velocity of the powder and promote plastic deformation bonding,[33,34] addressing the difficulty of depositing high-hardness materials using conventional CS.[35]

Existing research has shown that LACS can significantly improve the quality of Ti and Ti alloy coatings. Boruah *et al.*[36] demonstrated that during CS deposition of Ti6Al4V, the LACS process reduced coating porosity from 2.3% in conventional CS to 0.4%, with a significantly enhanced interfacial bonding. This result indicates that laser preheating can effectively eliminate inherent pores in CS and improve coating density and cohesive strength. Furthermore, Birt *et al.*[37] systematically optimized parameters using a statistical orthogonal design and successfully achieved LACS deposition of Ti6Al4V powder on a Ti6Al4V substrate using nitrogen as a carrier gas, achieving a coating porosity below 1%, equivalent to the deposition quality of expensive helium CS. The aforementioned work also found that the microstructure and morphology of the coating can be controlled during the LACS process by adjusting process parameters such as laser power, spraying speed, and powder feed rate; meanwhile, the substrate preheating temperature and spray track spacing are key factors affecting LACS coating quality. However, there is currently almost no research on the formation mechanism and performance of Ti6Al4V coatings deposited on 6061Al by LACS.

This study investigates the effect of laser power on the preparation and performance of Ti6Al4V coatings deposited on 6061Al substrates via LACS. The microstructure, phase composition, and mechanical properties of the coatings were characterized and compared, and the deposition mechanism of Ti6Al4V powder particles during the LACS process was further studied through electron backscatter diffraction (EBSD) and transmission electron microscopy (TEM). This research provides sufficient experimental data for the preparation of high-performance Al/Ti composites using LACS and contributes to advancing LACS technology in relevant fields.

2. Experimental methods

2.1. Materials

The substrates utilized in this study were commercial 6061Al plates (100 × 50 × 10 mm^3). These substrates were ultrasonically cleaned in ethanol for 20 min to remove impurities such as grease and dust, followed by laser surface micro-texturing to remove the oxide film and enhance surface roughness, which is conducive to particle bonding. A final 20-min ultrasonic cleaning in ethanol was then performed. These pretreatment steps were performed only once before the spraying process and were not repeated during subsequent deposition cycles. Experiments were conducted within 2 h of substrate treatment, and the elemental composition is provided in Table 1. The raw material consisted of gas-atomized Ti6Al4V powder (Jinggao Advanced Material Technology Co., Ltd., China), featuring spherical particles within a size range of 15–53 μm (Figure 1). Prior to the experiments, the metal powder was dried in a vacuum oven to eliminate moisture and improve powder flowability. The drying temperature was set at 110 °C with a heating rate of 5 °C/min. Upon reaching the target temperature, the powder was held for 2 h while the vacuum degree was maintained at 0.06 MPa.

2.2. Laser-assisted cold spray process

The schematic of the LACS system is illustrated in Figure 2. The system primarily comprises a high-pressure nitrogen station, a high-pressure CS system (PCS-1000, Plasma Giken, Japan), a laser system, a six-axis robotic arm system, and a sample stage. The laser head and De-Laval nozzle are mounted on the robotic arm (Staubli TX200L, Switzerland) at an angle of 30° relative to the vertical plane. The semiconductor-coupled fiber laser (Laserline LDF6000-100VGP, Germany) operates at a wavelength of 1,060 nm, with a spot diameter of 6 mm and a Gaussian intensity distribution. In this study, nitrogen was utilized as the acceleration gas, with laser power ranging from 0 to 800 W. The detailed process parameters are summarized in Table 2. The Ti6Al4V deposits were fabricated by depositing two successive layers under identical processing conditions, resulting in a coating thickness suitable for subsequent microstructural and mechanical characterization.

2.3. Microstructural and phase characterization

2.3.1. Coating morphology characterization

In this study, scanning electron microscopy (SEM; ZEISS Sigma HV-01-043, Germany) was employed to observe and analyze the interface between the Ti6Al4V coating and the substrate. The preparation method for the cross-sectional etched samples was as follows: representative samples of appropriate size were cut using an electrical-discharge wire machine. The samples and resin powder were placed into a hot-mounting machine, where they underwent heating, pressurization, and cooling to solidify the resin. The mounted samples were ground using 80, 240, 400, 800, 1,500, and 2,000 grit sandpapers. Finally, the sample surfaces were polished to a mirror finish using a 2.5 μm diamond polishing agent and a velvet polishing cloth. The samples were etched using Kroll's reagent ($HF:HNO_3:H_2O$ = 1 mL:2 mL:50 mL) for 10 s, followed by rinsing to remove the etchant, cleaning with ethanol, and blow-drying to observe the internal interfacial characteristics of the coating.

Electron backscatter diffraction (Symmetry S3, Oxford Instruments, United Kingdom) was used to analyze the grain orientation and distribution of the coatings. A scanning step size of 60 nm and a voltage of 20 kV were applied during EBSD measurements. Data processing and analysis were performed using the AZtecCrystal (Version 2.1, Oxford Instruments, United Kingdom) software. TEM samples were extracted from the cross-section of the bonding interface between the deposited particles and the substrate using a focused ion beam (FIB) dual-beam microscope (Helios G5 CX, Thermo Fisher Scientific, United States of America [USA]). The initial sample size was 10 × 8 μm with a thickness of approximately 1 μm, which was then milled to approximately 90 nm using a Ga-ion beam. A transmission electron microscope (Tecnai G2 F30 STWIN, FEI, Netherlands) was utilized to characterize and analyze the interfacial microstructure

Table 1. Chemical composition of commercial 6061Al substrate

Element	Al	Mg	Si	Fe	Cu	Cr	Zn	Mn	Ti
Content (wt.%)	Balance	1.00	0.60	0.35	0.28	0.20	0.10	0.08	0.05

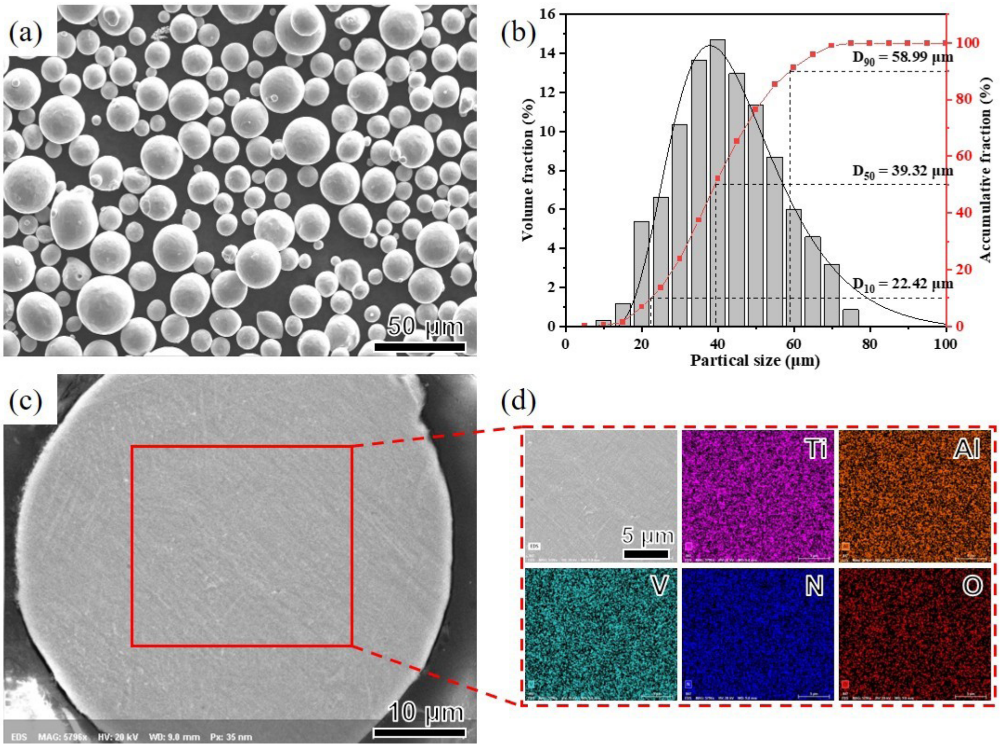

Figure 1. Ti6Al4V powder. (a) Scanning electron microscopy (SEM) image of overall powder morphology. Scale bar: 50 μm; magnification: 5,000×. (b) Particle size distribution. (c) SEM image of a particle cross-section. Scale bar: 10 μm; magnification: 5,000×. (d) Magnified view with energy-dispersive spectroscopy (EDS) mapping showing solute element distribution. Scale bars: 5 μm; magnifications: 5,000×.

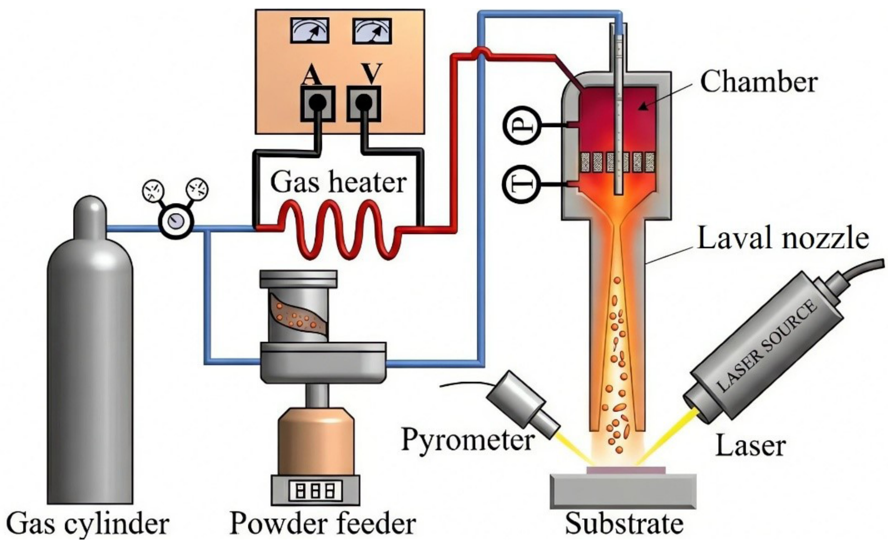

Figure 2. Schematic illustration of the laser-assisted cold spray (LACS) system

Table 2. Laser-assisted cold spray processing parameters

Coating	Laser power (W)	Gas temperature (°C)	N_2 pressure (MPa)	Spray distance (mm)	Powder feeding speed (r/min)	Spray speed (mm/s)
1	0	800	4	30	2	50
2	400					
3	600					
4	800					

between the particles and the substrate.

2.3.2. Phase characterization of the coating

Energy-dispersive spectrometry (EDS; Bruker Nano Xflash Detector 5010, Germany) was used to examine elemental distribution across the coating–substrate interface by area (elemental mapping) and line scanning (elemental concentration variation). An X-ray diffractometer (XRD; ARL ADVANT'X 4200, USA) was employed for phase identification of the original Ti6Al4V powder and the deposited layers produced under different processing conditions (CS, LACS-400 W, LACS-600 W, and LACS-800 W).

Measurements of XRD were carried out using Cu Kα radiation (λ = 1.5406 Å) at 40 kV and 100 mA, with a scan speed of 2°/min, a step size of 0.02°, and a 2θ range of 30–80°. Diffraction peaks were indexed according to the standard Ti6Al4V reference card (PDF#44-1294) to determine the phase composition. To extract microstructural information from the peak broadening β, the Williamson–Hall (W–H) method[38] was adopted to deconvolute the contributions of crystallite size and microstrain. Prior to analysis, instrumental broadening was corrected as follows:

$$\beta = \sqrt{\beta_{obs}^2 - \beta_{inst}^2} \quad (1)$$

where β_{obs} is the measured full width at half maximum (FWHM), β_{inst} is the instrumental broadening, and β is the corrected peak broadening. All values were converted into radians. The W–H linear relationship was then expressed as:

$$\beta\cos\theta = \frac{K\lambda}{D} + \varepsilon\sin\theta \quad (2)$$

where θ is the Bragg angle, K is the shape factor (0.9 in this work), D is the average coherent diffraction domain size, and ε is the average lattice microstrain. Multiple diffraction peaks were selected, and the corresponding values of $\beta\cos\theta$ and $\sin\theta$ were calculated for linear fitting. The intercept $K\lambda/D$ was used to determine D, and the slope corresponded to ε.

2.4. Mechanical testing

Microhardness measurements were conducted using a Vickers hardness tester (HMV-2TADWXY, Shimadzu, Japan), and the sample surface was ensured flat prior to testing. A test load of 1.96 N and a dwell time of 15 s were applied. For each processing condition, 10 indentations were recorded to obtain the average value and standard deviation. In accordance with ASTM C1327, indentation diagonals were calibrated under 4× optical magnification.

Adhesive pull-off tests were performed in accordance with ASTM C633[39] on a universal testing machine (UTM5105SYXL, Shenzhen Sansi Zongheng Technology Co., China) at a constant tensile rate of 0.3 mm/min to evaluate coating–substrate bonding strength. The deposited coating and substrate were sectioned into cylindrical specimens with a diameter of 25 mm and ultrasonically cleaned in ethanol for 10 min to remove grease. An E-7 epoxy adhesive (Shanghai Synthetic Resin Institute, China) was applied to bond the specimen to the pull-off fixtures on both sides, followed by curing under pressure at 180 °C for 3 h. Three specimens were prepared for each set of processing parameters to ensure reproducibility.

The tensile specimens were prepared and tested in accordance with ASTM E8/E8M, "Standard Test Methods for Tension Testing of Metallic Materials." Dog-bone tensile specimens were machined from the deposited layer using electrical-discharge wire cutting, with dimensions of 30 × 5 × 2 mm^3. Both sides of each specimen were ground using 2,000-grit SiC paper and ultrasonically cleaned in ethanol. Tensile tests were performed at room temperature using a servo-controlled universal tensile machine (CMT5504, Shenzhen Sansi Zongheng Technology Co.), and elongation was measured using a laser extensometer (laserXtens, ZwickRoell, Germany). The tensile speed was set to 0.1 mm/min. Three specimens were tested for each condition to ensure repeatability.

2.5. Statistical analysis

In this study, quantitative characterization of the porosity and particle aspect ratio of the Ti6Al4V deposits was conducted using image analysis. Specifically, more than 10 representative cross-sectional regions from each deposit were randomly selected for SEM imaging. The acquired images were subsequently processed using ImageJ (version 1.54, National Institutes of Health, USA) for grayscale threshold segmentation. Porosity was defined as the ratio of the pore area to the total pixel area, and the arithmetic mean of all sampled regions was adopted as the final porosity for each processing parameter. Regarding the particle aspect ratio, the long axis (width, D) and short axis (height, d) of the deposited particles were measured using ImageJ, and the aspect ratio was calculated as d/D. A minimum of 30 particles per sample were statistically analyzed, and the average value was taken as the final aspect ratio.

3. Results

3.1. Microstructure

The cross-sectional morphologies of the Ti6Al4V deposits on the 6061Al substrate under different laser powers are shown in Figure 3. Cross-sectional observations revealed a distinct stratified morphology along the thickness direction, which was divided into three characteristic regions: a bottom region adjacent to the substrate, a middle deposition zone, and a top region. All samples exhibited similar features in the bottom region: numerous particles retained their original spherical morphology, local plastic flattening was insufficient, and unclosed interparticle gaps, particle–substrate gaps, and point-like pores remained along the interface. Even with laser preheating in LACS, densification improvement in this bottom layer remained limited.

This phenomenon can be interpreted from the perspective of impact energy dissipation pathways coupled with dynamic mechanical response. During high-velocity impact, plastic flow and a localized temperature rise at the particle–substrate interface occur on the microsecond timescale. The associated shear energy is prone to adiabatic shear localization;[40] however, the thermal softening produced by adiabatic shear localization is confined within an extremely thin shear band around the particle/interface and does not translate into full-particle softening. Meanwhile, Ti6Al4V exhibits pronounced strain-rate hardening, elevating its dynamic flow stress. As a result, local shear softening does not evolve into extensive macroscopic flattening; instead, particles tend to complete impact through a "localized dissipation–elastic rebound" response, preserving a near-spherical profile in cross-sections.

In addition, the high thermal conductivity and elastic-wave transmission of the 6061Al substrate allow impact energy to be rapidly absorbed and dispersed, suppressing interfacial temperature rise and reducing substrate-surface softening. This limits interfacial plastic flow and bonding. The substantial contrast in hardness and yield strength between Ti6Al4V and 6061Al further amplifies this "rigid-receptor" effect,[41] making it difficult for incoming Ti6Al4V particles to undergo large-scale plastic deformation. Lastly, considering that 6061Al has high reflectivity at 1,064-nm infrared laser radiation,[42] the substrate absorbs limited laser energy during rapid scanning. Consequently,

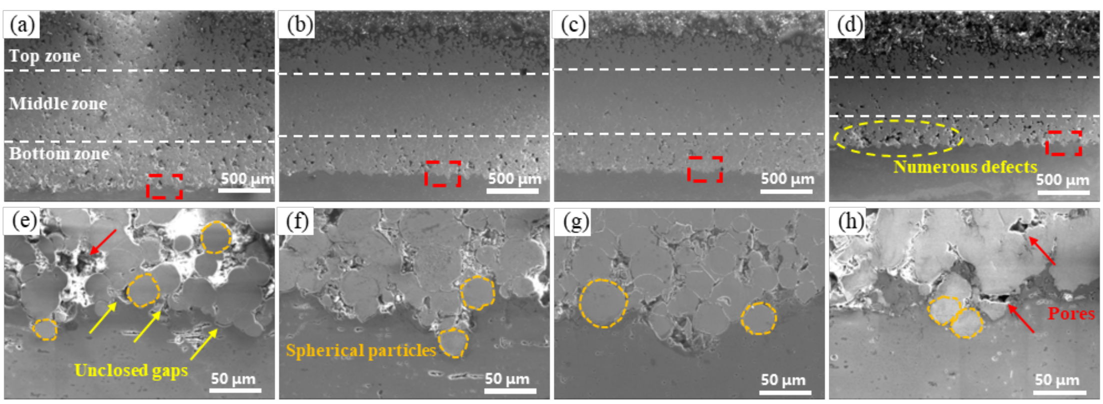

Figure 3. Cross-sectional morphologies of the deposited layer and substrate under different laser powers: (a) cold spray (CS), (b) laser-assisted CS (LACS)-400 W, (c) LACS-600 W, (d) LACS-800 W, and (e–h) corresponding magnified views. Scale bars: (a–d) 500 μm, (e–h) 50 μm; magnifications: (a–d) 100×, (e–h) 1,000×.

insufficient thermal accumulation occurs at the particle impact moment, and the contribution of laser preheating to lowering the critical deposition velocity and promoting interfacial softening is weakened in the bottom region.

The cross-sectional morphology of the mid-thickness deposition zone under different laser powers is shown in Figure 4. As observed morphologically (Figure 4a–d), in the CS sample, particle boundaries remained sharp, interparticle necking was scarce, and numerous interconnected or isolated pores were visible. At 400 W, porosity in the middle layer was substantially reduced, with increased plastic flow and neck formation between particles, though discontinuous microcracks remained. The LACS-600 W coating exhibited the most continuous and densified structure, characterized by blurred particle boundaries, extensive particle flattening and necking, and nearly complete pore closure. At 800 W, porosity increased slightly, which may be attributed to oxidation or partial particle ablation induced by excessive thermal input, thereby degrading deposition performance, although a high level of densification was still maintained.

Quantitative analysis of coating porosity and particle aspect ratio further confirms these observations. As the laser power increased from 0 to 600 W, porosity decreased from 11.87% to a minimum of 0.41%, and the particle aspect ratio decreased from 0.81 to 0.52, demonstrating that particle plastic flattening is the key factor governing pore elimination and microstructural densification.

3.2. Phase analysis

Figure 5 presents the XRD patterns of the Ti6Al4V feedstock powder and the coatings deposited under different processing conditions. The diffraction peak positions of all deposited samples remained consistent with those of the original powder, and all peaks were indexed to hexagonal close-packed α-Ti. Within the scanned 2θ range and instrumental sensitivity, no characteristic peaks corresponding to body-centered cubic β-Ti were detected. Likewise, within the detection sensitivity of XRD, no new diffraction peaks associated with Al/Ti intermetallic compounds (e.g., $TiAl_3$, TiAl, Ti_3Al) were observed under any processing condition.

Differences between the deposited coatings and the powder primarily manifest as slight peak broadening and intensity variation, which can be attributed to high-strain-rate plastic deformation during cold spraying, grain refinement, and increased dislocation density, rather than the formation of new phases. These observations indicate that, within the applied laser-power window, LACS still follows a predominantly solid-state deposition mechanism. The laser did not induce significant localized melting/resolidification, nor did it trigger α→β phase transformation or generate substantial amounts of brittle Al/Ti intermetallics. Accordingly, the original phase constitution of the feedstock was effectively preserved. This behavior highlights the stability and advantages of LACS in dissimilar-metal additive manufacturing, helping to avoid brittle-phase aggregation and high-temperature phase transitions typically encountered in fusion-based alloy systems.

3.3. Grain morphology, size, and recrystallization

Grain-structure evolution was examined using EBSD, including grain size, morphology, and boundary

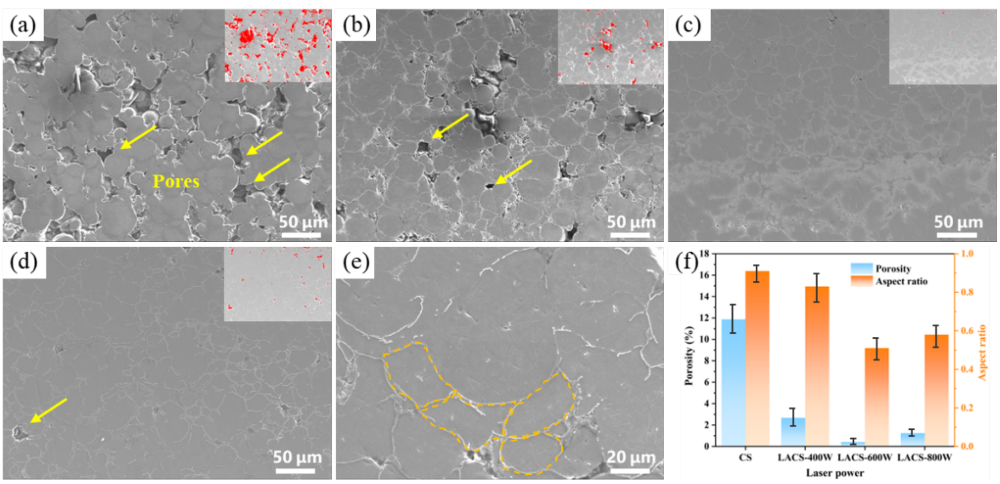

Figure 4. Cross-sectional morphologies of the mid-thickness Ti6Al4V deposition zone under different laser powers: (a) cold spray (CS), (b) laser-assisted CS (LACS)-400 W, (c) LACS-600 W, and (d) LACS-800 W. (e) Particle aspect-ratio statistics. (f) Variation in coating porosity and particle aspect ratio. Scale bars: (a–d) 50 µm, (e) 20 µm; magnifications: (a–d) 500×, (e) 1,000×.

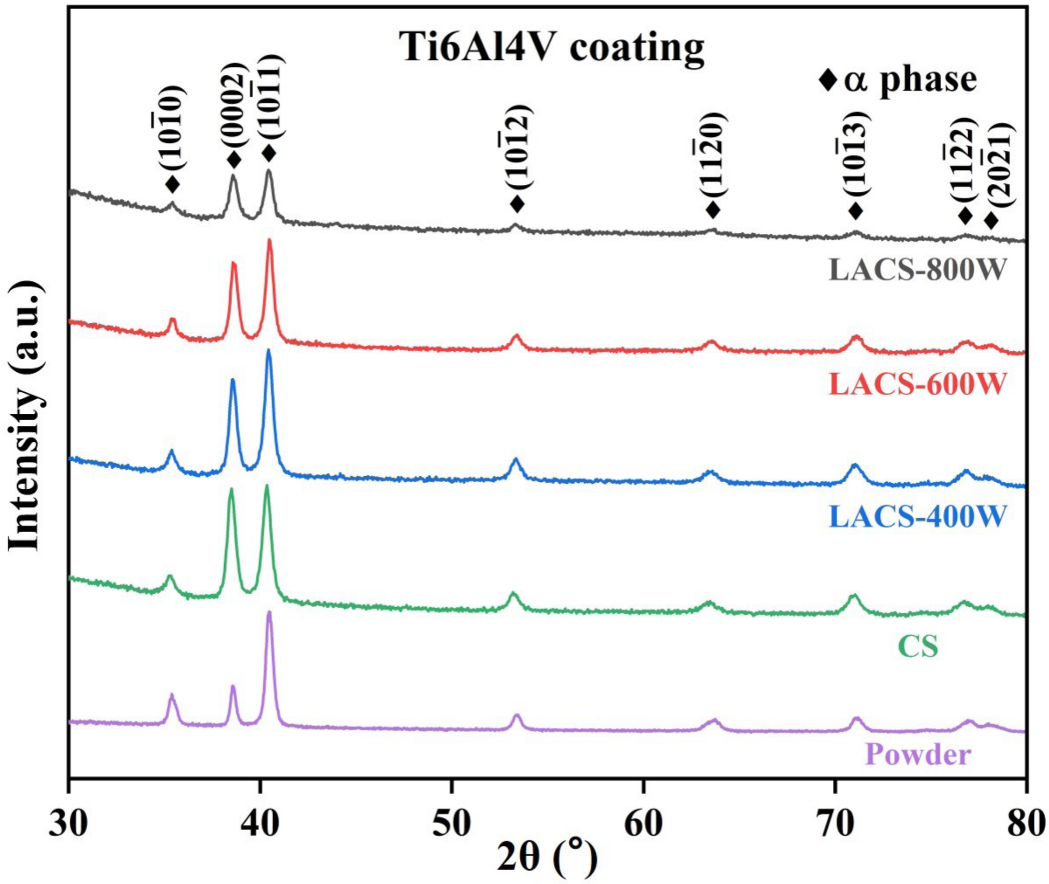

Figure 5. X-ray diffraction (XRD) patterns of Ti6Al4V powder and coatings deposited under different processing conditions

characteristics (Figure 6). Figure 6a and 6b presents the inverse pole figure (IPF) maps of the CS and LACS-600 W samples, respectively, and Figure 6c and 6d shows the corresponding grain size distributions. A marked refinement effect was observed in the deposited microstructure. Within an identical mapped area, the CS sample exhibited elongated grains through the central particle region with strong directional texture (an apparent banded/strip-like grain morphology), whereas fine equiaxed grains and more random orientations typically appeared near particle edges and interparticle contact zones.

With laser assistance, the grain morphology became more equiaxed and uniform in size, the color distribution became finer without extended directional features, and the average grain size decreased significantly (1.906 → 0.813 μm). In conventional CS, the high-velocity particle impact produced severe plastic deformation; shear and localized strain concentration along particle edges generated high dislocation densities and subgrain structures, yielding much finer grains in these regions. In contrast, the particle interior—particularly where extreme plastic deformation did not occur—retained relatively coarse original grains, resulting in a microstructure characterized by fine-grained rims and coarse, directionally elongated cores. During LACS, transient and localized thermal input coupled with plastic deformation produced two critical effects: (i) enhancement of dynamic recovery/recrystallization tendencies, and (ii) promotion of new-grain nucleation and refinement. Consequently, the microstructure transitioned from heterogeneous elongated/deformed grains to a more uniform array of fine equiaxed grains.

Figure 7 displays the grain-boundary distribution, grain orientation spread (GOS), and kernel average misorientation (KAM) characteristics of the CS and LACS-600 W coatings, further demonstrating the role of LACS in promoting dynamic recrystallization and microstructural refinement. With respect to grain-boundary types, the CS sample (Figure 7a) exhibited 25.4% low-angle grain boundaries (LAGBs; 2°–15°) and 74.6% high-angle grain boundaries (HAGBs; >15°). In contrast, the LACS-600 W sample (Figure 7d) exhibited a reduced LAGB fraction

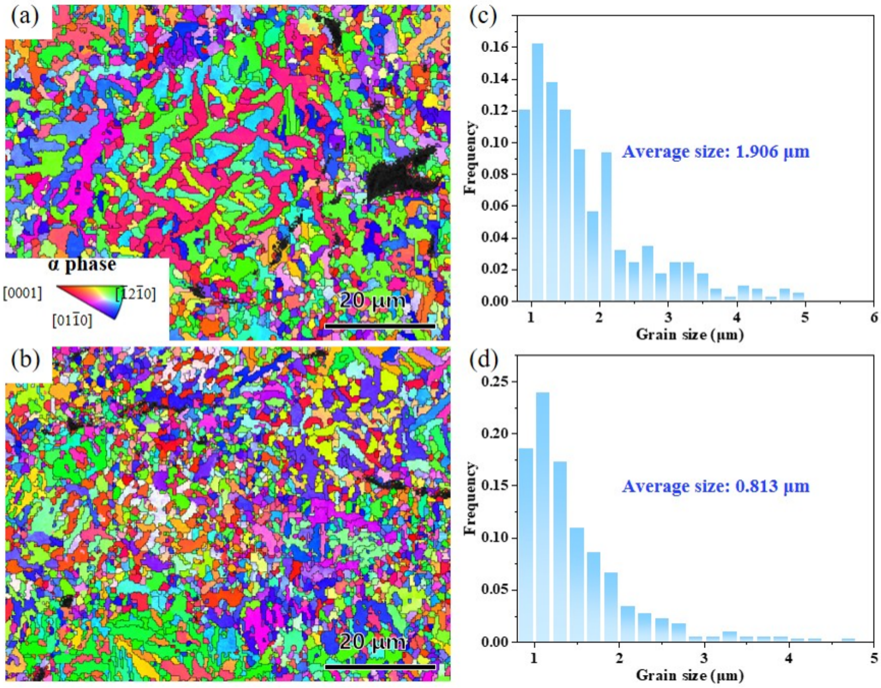

Figure 6. Electron backscatter diffraction (EBSD) images of the deposited layer: Inverse pole figure (IPF) maps of the (a) cold spray (CS) and (b) LACS-600 W samples. Scale bars: 20 μm; magnifications: 1,000×. (c–d) Corresponding grain-size distribution maps.

of 18.2% and an increased HAGB fraction of 81.8%. This evolution indicates that, under laser assistance, dislocation cells and subgrain boundaries originally represented as low-angle boundaries undergo further migration and lattice rotation, transforming into stable high-angle boundaries—consistent with the emergence of fine equiaxed grains.[43]

To further quantify the deformation–recovery–recrystallization state of Ti6Al4V under different processing conditions, GOS[44] was employed to evaluate the degree of intragranular orientation dispersion. GOS describes the deviation of each pixel's orientation within a grain from the average orientation of that grain, thereby reflecting accumulated intragranular plastic deformation and lattice distortion at the grain scale. For the i-th grain (containing J_i pixels), GOS can be expressed as:

$$GOS(i) = \frac{1}{J_i}\sum_{j=1}^{J_i}\omega_{ij} \quad (3)$$

where ω_{ij} represents the minimum misorientation angle between pixel j within a grain and the average orientation of that grain. In general, a higher GOS value indicates a stronger intragranular orientation gradient, implying more severe plastic deformation and a higher level of residual lattice misorientation. Conversely, low GOS values typically correspond to grains formed through sufficient recovery or dynamic recrystallization, exhibiting more uniform orientations.

Based on the GOS maps (blue: GOS < 2°, defined as dynamically recrystallized grains; yellow: 2°–7°, recovery grains; red: GOS > 7°, deformed grains), clear differences were observed between CS and LACS-600 W specimens. In the CS sample, the fraction of dynamically recrystallized grains was only 18.05%, whereas recovery grains dominated (68.79%) and a non-negligible fraction of deformed grains remained (13.16%). This indicates that microstructural evolution during conventional cold spraying is largely recovery-dominated, and substantial intragranular orientation dispersion and residual deformation persist. By contrast, in the LACS-600 W sample, the fraction of dynamically recrystallized grains increased markedly to 38.35%, while recovery grains decreased to 57.41% and deformed grains dropped to 4.24%. These results demonstrate that under laser assistance, the deposited microstructure transitions from a recovery/deformation-dominated state toward a dynamic-recrystallization–dominated regime.

Kernel average misorientation[45] was used to quantify local orientation variation between neighboring EBSD pixels, serving as an indicator of local plastic deformation and a proxy for the density of geometrically necessary dislocations or stored dislocation energy. Higher KAM values signify stronger local misorientation, greater intragranular heterogeneity, and more pronounced plastic strain accumulation or higher dislocation density; conversely, lower KAM values imply weakened local orientation gradients and partial dislocation annihilation, rearrangement, or recovery, reflecting reduced stored strain energy and a more homogeneous intragranular strain distribution.

As shown in Figure 7c, the average KAM value of the CS sample was 0.71°, with numerous regions exhibiting elevated KAM, indicating strong local orientation fluctuations and retained internal strain after deposition. With laser assistance, however, the average KAM value in the LACS-600 W coating decreased to 0.53°, with a more uniform low-KAM distribution (Figure 7f). This suggests that the thermal activation or "annealing" effect of laser assistance promotes dislocation glide, annihilation, and rearrangement, enabling partial release of local strain and reducing intragranular orientation nonuniformity. Importantly, the reduction in KAM does not imply insufficient plastic deformation; rather, it indicates that under coupled laser–impact loading, deformation energy is more effectively consumed or transformed through recovery and dynamic recrystallization.

This interpretation is consistent with the increased HAGB fraction observed in the grain-boundary statistics. The concurrent increase in high-angle boundaries and decrease in KAM is a typical signature of recrystallization, in which low-dislocation, uniformly oriented new grains replace high-dislocation–density deformed regions. Thus, from the perspective of defect-state evolution, the results further confirm that laser assistance enhances dynamic recrystallization and promotes microstructural optimization, in agreement with the significant increase in the GOS-defined recrystallized-grain fraction.

3.4. Microhardness

Figure 8 shows the trend in microhardness of Ti6Al4V coatings under different laser powers. As the laser power increased from 0 W (CS) to 800 W, the coating hardness rose from 316.2 $HV_{0.2}$ to 388.1 $HV_{0.2}$, representing an overall increase of nearly 23%. This trend is highly consistent with the microstructural and EBSD observations discussed earlier. In the conventional CS sample, grains remained relatively coarse, porosity was high, and a considerable

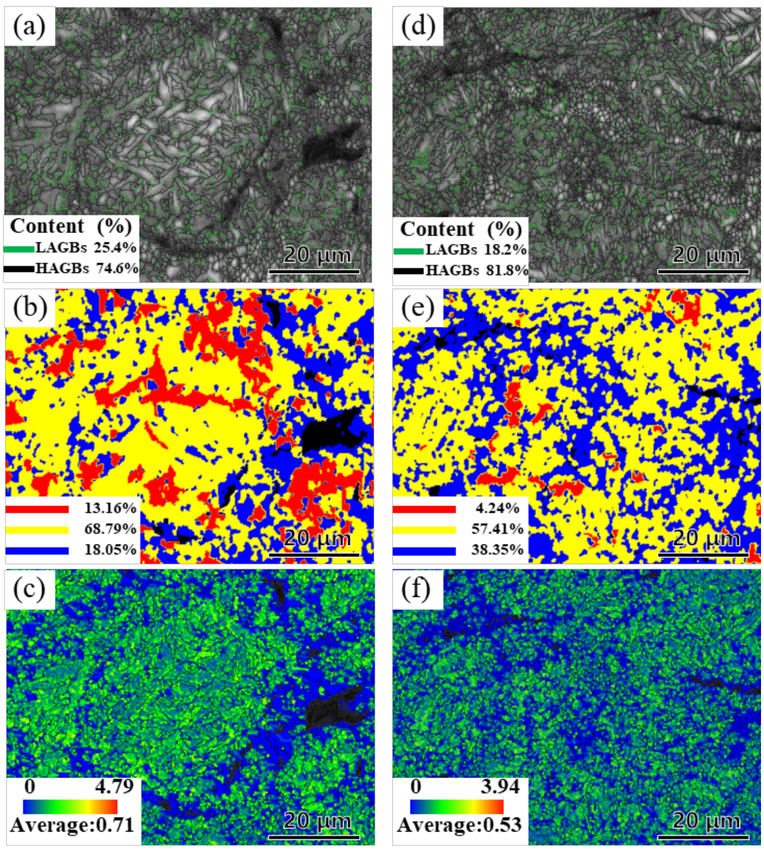

Figure 7. Grain-boundary maps, grain orientation spread (GOS) maps, and kernel average misorientation (KAM) maps of the deposited layers: (a–c) Cold spray (CS) sample, and (d–f) laser-assisted CS (LACS)-600 W sample. Scale bars: 20 μm; magnifications: 1,000×.

fraction of incompletely recovered deformed grains persisted. Although deformation introduced dislocation strengthening, its effect was partially offset by high porosity and interfacial defects, resulting in the lowest hardness.

Upon laser assistance at 400 W, porosity in the intermediate layer was substantially reduced, particle flattening improved, and more interparticle necks formed, increasing hardness to 357.7 $HV_{0.2}$. At 600 W, the coating attained its most densified structure (lowest porosity), the finest equiaxed grains, and the highest fraction of high-angle boundaries and dynamically recrystallized grains—reflecting typical grain-refinement and grain-boundary strengthening effects.[46] The microhardness thus increased to 377.5 $HV_{0.2}$. Meanwhile, the reduced KAM value indicates partial release of residual strain, although fine grains and uniformly distributed dislocations remain effective barriers to dislocation motion.

At 800 W, hardness increased slightly further to 388.1 $HV_{0.2}$, indicating that higher laser power can continue to provide localized strengthening (e.g., additional plastic deformation and residual-stress contributions). However, considering the increased porosity and interfacial defects noted earlier, localized microcracking and defect clusters were observed under this condition, and the overall mechanical performance was inferior to that at 600 W.

3.5. Bonding strength

Figure 9 presents the coating–substrate bonding strength for the CS and LACS-600 W samples. Three specimens were prepared for each processing condition, and the pull-off tests were conducted using an adhesive-bonding method. In terms of nominal values, both groups fell within the same order of magnitude (55–70 MPa). However, the failure modes differed significantly between the two processes. In the CS group, one specimen (CS-2) failed at the coating–substrate interface, whereas the remaining two CS specimens and all three LACS-600 W specimens failed within the adhesive layer, indicating that under laser-assisted conditions, the true interfacial strength exceeds the strength of the adhesive layer.

Combined with the earlier layer-resolved cross-sectional observations, it can be inferred that although laser assistance has limited influence on the flattening of bottom-layer particles adjacent to the 6061Al substrate and does not substantially eliminate interfacial porosity—meaning that mechanical interlocking remains the dominant bonding mechanism—the nominal interfacial strength does not vary dramatically between the two processes. Nonetheless, in LACS-600 W samples, the mid-thickness deposit exhibited drastically reduced porosity, enhanced particle flattening, refined grains, and an increased fraction of recrystallized grains. These improvements significantly enhance the

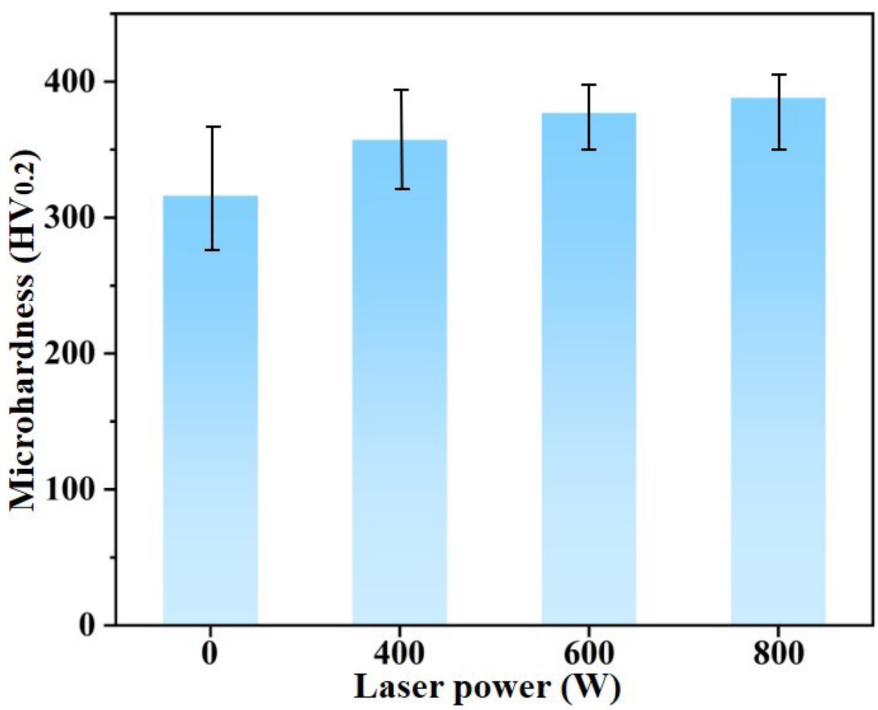

Figure 8. Microhardness variation of deposited layers under different laser powers

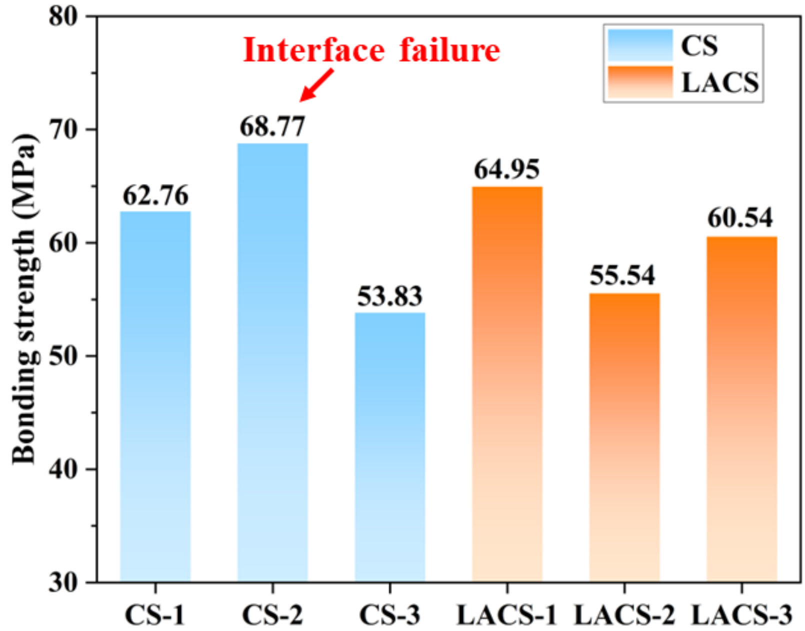

Figure 9. Bonding strength tests for specimens prepared under cold spray (CS) and laser-assisted CS (LACS)-600 W samples

load-bearing capability and stress-transfer uniformity of the coating. As a result, interfacial stress concentrations and weak-zone sensitivity are mitigated, and interfacial debonding is no longer the dominant failure mode. It must be emphasized that the measured pull-off strengths (55–70 MPa) are strictly dictated by the performance threshold of the epoxy adhesive, representing an adhesive-limited strength rather than the true quantitative coating–substrate interfacial bonding strength. In this study, partial interfacial debonding was observed in the conventional CS group; all LACS specimens failed cohesively within the glue layer. This failure mode transition indicates that the true interfacial strength of the LACS coating exceeds the current adhesive threshold (~70 MPa). Consequently, while the present pull-off data cannot quantitatively calculate the precise increase in true interfacial strength due to these adhesive limitations, the complete elimination of interfacial debonding qualitatively demonstrates a significant improvement in the lower bound of bonding reliability for the LACS-ed Ti6Al4V–6061Al interface.

3.6. Tensile properties

While the interfacial bonding strength between the coating and the substrate was independently evaluated via pull-off tests in Section 3.5, tensile testing was further conducted to investigate the intrinsic bulk mechanical properties of the deposited Ti6Al4V layers. Figure 10b depicts the engineering stress–strain curves of the tensile specimens obtained from the Ti6Al4V deposits under CS and LACS-600 W conditions. Figure 10c presents the comparison of the tensile properties for all tested samples. The conventional CS samples exhibited ultimate tensile strengths (UTS) ranging from 130 MPa to 170 MPa, with an average of 145.03 MPa and an average elongation of only 1.10%. In contrast, in LACS-600 W, the three specimens reached an average UTS of 206.58 MPa, and the average elongation increased to 2.17%. In other words, with appropriate laser assistance, the deposit strength improved by roughly 40%, and ductility nearly doubled.

From a micromechanical standpoint, the strength enhancement in the LACS-600 W samples is closely associated with grain refinement. According to the Hall–Petch relationship,[47] the yield strength of polycrystalline materials correlates with grain size d through the following empirical expression:

$$\sigma_y = \sigma_0 + k_y d^{-\frac{1}{2}} \tag{4}$$

where σ_y is the yield strength (which generally scales with overall strength levels), σ_0 is the lattice friction stress associated with intragranular dislocation glide, and k_y is the Hall–Petch slope reflecting the ability of grain boundaries to impede dislocation motion. This relation indicates that as grain size d decreases, $d^{-1/2}$ increases, and grain-boundary strengthening becomes more pronounced. Based on the EBSD grain-size statistics, the average grain size in the CS deposit was 1.906 μm, whereas that in LACS-600 W was refined to 0.813 μm. The associated increase in $d^{-1/2}$ therefore provides a rational source of strengthening in the LACS sample. Beyond grain refinement, the LACS-600 W coating contained a higher fraction of HAGBs and a more homogeneous deformation–recrystallization microstructure, both of which further elevated resistance to dislocation glide and suppressed local strain concentrations. Meanwhile, the substantial reduction in porosity and the improvement in interparticle bonding mitigated early damage nucleation and stress concentration, enabling the coating to sustain higher applied loads and achieve greater elongation during tensile deformation.

Figure 10d compares the tensile performance of LACS-ed Ti6Al4V with reported data for conventionally CS-ed Ti6Al4V.[14,48-52] The Ti6Al4V coatings fabricated in this work using N_2 as the carrier gas exhibited significantly improved strength and ductility relative to published N_2-based CS samples, representing a clear shift from the low-strength/low-ductility domain toward a higher-performance regime.

The tensile fracture morphologies of the CS and LACS-600 W samples are presented in Figure 11. Significant differences in the fracture characteristics can be observed between the two deposition conditions. For the CS sample (Figure 11a), the fracture surface exhibited numerous retained particle contours, interparticle gaps, and particle pull-out features. The fracture path predominantly followed particle boundaries, indicating that failure is governed by weak interparticle bonding and residual defects. Such fracture characteristics are consistent with the relatively high porosity and limited particle deformation observed in the microstructural analysis. In contrast, the LACS-600 W sample (Figure 11b) displayed a much denser fracture surface with substantially reduced particle pull-out features. The original particle morphology became less distinguishable, while the fracture path became noticeably more tortuous. Extensive interparticle fracture accompanied by localized tearing features was observed, suggesting that stronger interparticle bonding was established during laser-assisted deposition. As a result, crack propagation required higher energy and proceeded through a more complex path.

These fractographic observations provide direct evidence that improvements in tensile strength and elongation are closely associated with enhanced particle bonding, reduced porosity, and a more homogeneous

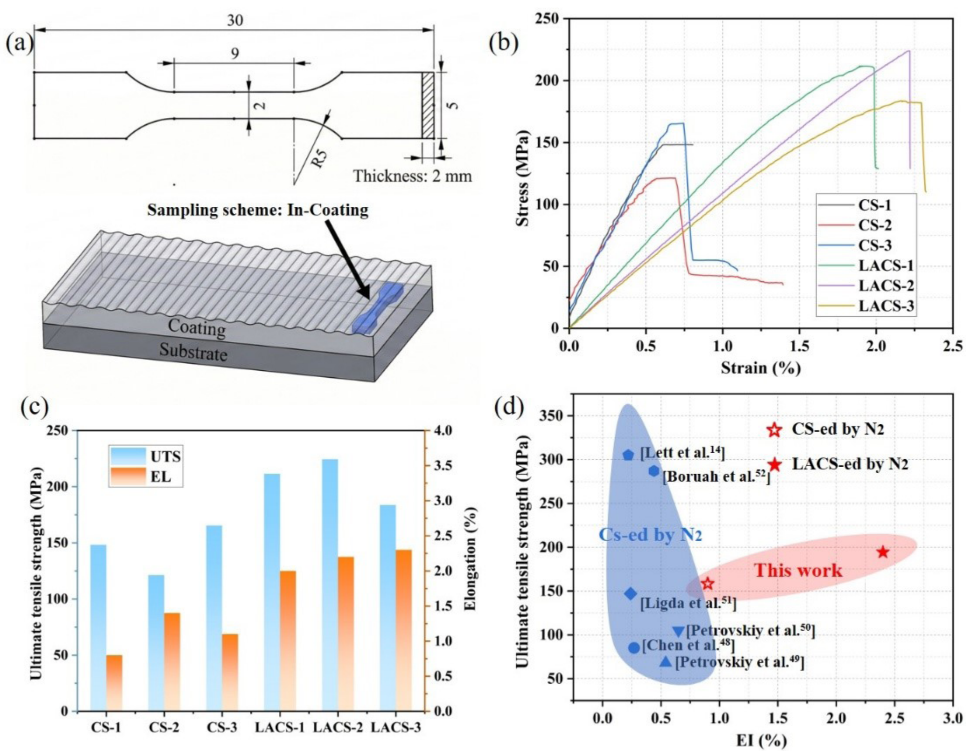

Figure 10. Tensile properties of cold spray (CS) and laser-assisted CS (LACS)-600 W deposits. (a) Schematic of tensile specimen sampling. (b) Engineering stress–strain curves of CS and LACS-600 W samples. (c) Tensile performance test results of CS and LACS-600 W samples. (d) Comparison of mechanical properties with other cold-sprayed Ti6Al4V deposits.

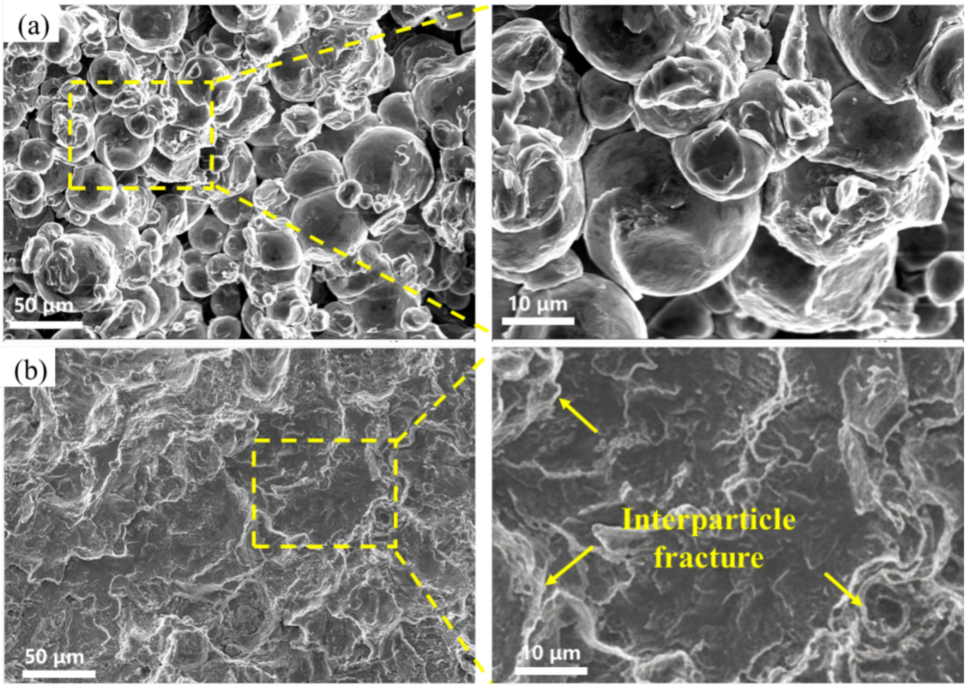

Figure 11. The tensile fracture morphology of the Ti6Al4V deposition layer under different process conditions: (a) cold sprat (CS), and (b) laser-assisted CS (LACS)-600 W. Scale bars: (left panels) 50 μm, (right panels) 10 μm; magnifications: (left panels) 1,000×, (right panels) 3,000×.

microstructure generated under LACS conditions. The suppression of premature crack initiation at weak particle interfaces enhances the load-bearing capacity and deformation resistance of the deposited material.

4. Discussion

4.1. Hypothesized formation mechanism of longitudinal stratification

Figure 3 illustrates that the Ti6Al4V deposition layer possesses stable longitudinal stratification characteristics along the thickness direction: the bottom region near the substrate showed insufficient particle flattening and obvious interfacial pores; the middle deposition layer achieved the best densification; and the top layer exhibited relative looseness again due to the weakened subsequent tamping effect. This longitudinal stratification may be interpreted using a proposed "laser irradiation-particle tamping synergistic mechanism," developed based on the observed microstructural evolution and deposition morphology,[53,54] as shown in the schematic diagram in Figure 12.

In the bottom region, the initially deposited particles directly affect the 6061Al substrate. Owing to the high thermal conductivity and high reflectivity of Al, the laser-induced heat is rapidly dissipated, resulting in insufficient thermal accumulation and limited thermal softening. Although the subsequently deposited particles still provide repeated tamping and compaction effects, the lack of sufficient thermal activation restricts particle flattening and pore closure. Consequently, the bottom region exhibits characteristic features of retained spherical particles and unclosed interfacial pores.

As the deposited layer thickness increases, the thermal conductivity of the receiving surface decreases, and laser energy can be accumulated more effectively. Simultaneously, the repeated impact of subsequently arriving particles generates a strong tamping effect. Therefore, laser-induced thermal softening and particle tamping act synergistically in the middle region, promoting extensive particle flattening, pore closure, and interparticle bonding. This synergistic effect produces the densest microstructure and the lowest porosity observed in the present study (corresponding to the lowest porosity and the lowest aspect ratio under the 600 W condition).

When deposition approaches the top free surface, although laser irradiation continues to provide thermal accumulation and local softening, the tamping effect from subsequently deposited particles becomes insufficient due to the absence of additional overlying layers. Consequently, particle rearrangement and pore closure become less effective, resulting in a slight increase in porosity and the formation of a relatively loose top region.

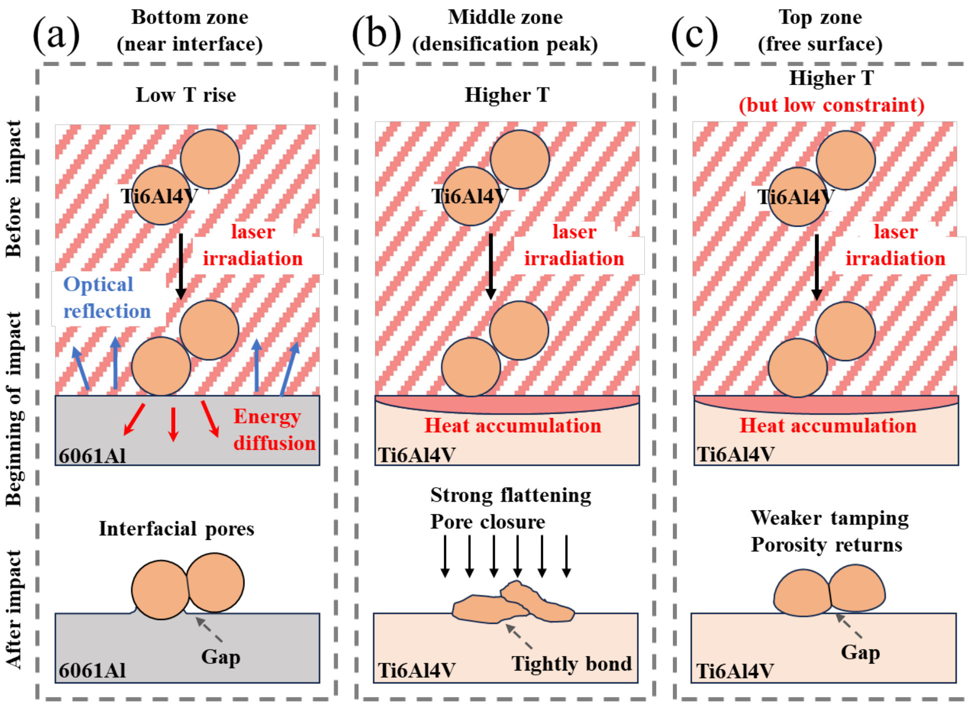

Figure 12. Schematic diagram of longitudinal stratified deposition: (a) bottom region; (b) middle region; and (c) top region

In summary, the distinct longitudinal stratification is a unique phenomenon exclusive to LACS of the highly thermophysically mismatched Ti6Al4V/6061Al system, contrasting sharply with the homogeneous microstructure typical of conventional CS (Figure 3a). This stratified evolution is hypothesized to originate from the synergistic effects of laser-induced thermal accumulation and particle tamping. Specifically, the bottom region is dominated by effective tamping but insufficient thermal accumulation; the middle region features synchronous thermal accumulation and tamping, achieving the highest density; while the top region undergoes thermal accumulation yet lacks sufficient subsequent tamping, leading to relatively porous structures. Driven by the extreme disparity in optical and thermophysical properties between the Al substrate and Ti particles, the boundary conditions shift from substrate-dominated rapid cooling at the bottom, through optimized thermal accumulation coupled with intense particle tamping in the middle, and ultimately transition to a loose, porous state with no tamping effect at the top.

4.2. Interfacial bonding mechanism of aluminum and titanium during laser-assisted cold spray

4.2.1. Grain refinement and gradient microstructural evolution at the interface

To further reveal the nanoscale bonding nature of Ti6Al4V particles and 6061Al matrix during the LACS process, high-resolution TEM samples at the interface were extracted by FIB, as shown in Figure 13a.

As shown in Figure 13b, at an observation scale of 500 nm, the edges of the Ti6Al4V particles were tightly bonded to the 6061Al substrate, with a flat interface and no microcracks. Since the average particle size of the original powder used in this study was 39 μm, the region shown in the figure only represents the intense plastic deformation zone at the extreme edge of the particle. Selected-area diffraction pattern analysis at different positions in the figure revealed that the diffraction rings exhibited obvious gradient characteristics: near the bonding interface (Position 1), the diffraction ring was the most complete and continuous, appearing as a smooth circular ring. This indicates that at the instant of impact, the interface experienced a coupling effect of extremely high strain rate and laser-assisted heat input, inducing thorough dynamic recrystallization. Severe shear deformation reduced the original grains to the nanometer level, and a large number of randomly oriented nanocrystals caused the diffraction spots to form a continuous ring.[55] Moving away from the interface toward the particle interior (Positions 2 and 3), as the distance from the interface increased, the diffraction ring gradually evolved from continuous to discontinuous spots (most obvious at Position 3). This trend corroborates the strain-gradient effect. Although Position 3 was only

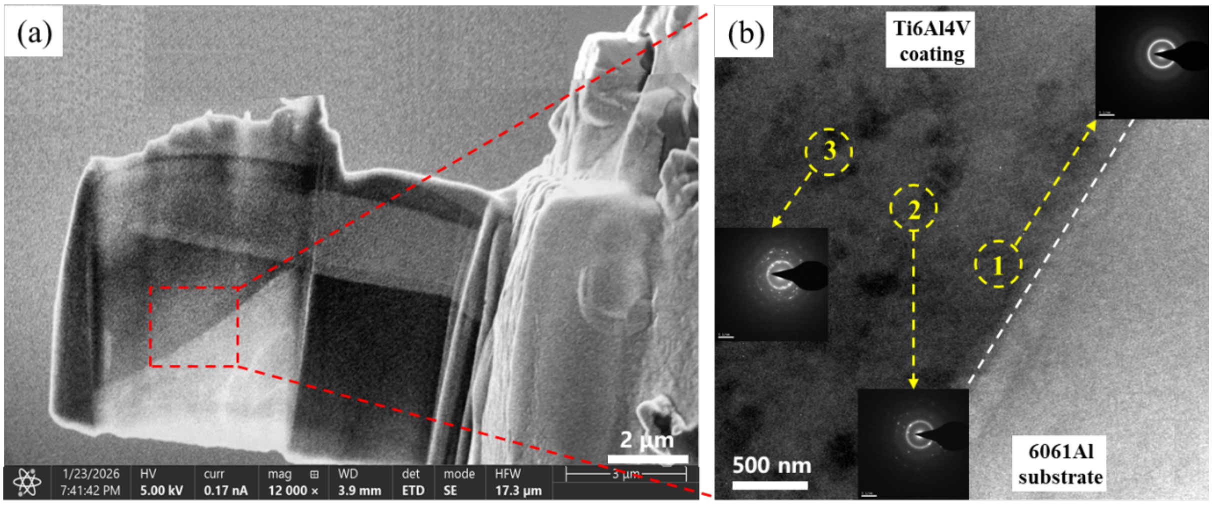

Figure 13. Interface microstructure of laser-assisted cold spray (LACS)-600 W sample. (a) Focused ion beam (FIB) sample preparation. Scale bar: 2 μm; magnification: 12,000×. (b) Transmission electron microscopy images and selected-area diffraction pattern images. Scale bar: 500 nm; magnification: 48,000×.

a few hundred nanometers from the interface, the shear energy generated by the CS impact decayed rapidly with increasing distance, reducing dislocation proliferation and the degree of grain fragmentation. Position 3 might be in a sub-crystallization stage transitioning from the original structure to nanocrystals, where the grain size was relatively large, leading to a decrease in the number of grains participating in diffraction and causing the spots to become discrete.

4.2.2. Nanoscale elemental redistribution and interfacial compositional gradation

Figure 14 presents the SEM–EDS results of the Ti6Al4V/6061Al heterogeneous interface in the LACS-600 W sample. It can be observed that Al was mainly distributed in the lower substrate region, whereas Ti and V were primarily enriched in the upper Ti6Al4V-deposited particles, indicating a relatively clear compositional partitioning across the interface. Meanwhile, a slight enrichment of O was detected near the interface, suggesting the possible presence of locally retained oxides or fragmented oxide films. The line-scan results showed that the Al and Ti signals varied continuously rather than abruptly across the interfacial region, indicating the existence of an elemental transition zone with a width of 5 μm. This suggests that a certain degree of elemental redistribution and compositional gradation occurred near the interface.[56]

The TEM–EDS results in Figure 15 further revealed that Ti and Al exhibited an overlapping distribution at the nanoscale near the interface, rather than forming an ideal sharp boundary. The TEM–EDS line scan further reflected the elemental variation within the interfacial transition zone. Along the scanning path crossing the heterogeneous interface, the Ti signal decreased markedly while the Al signal increased correspondingly when moving from the deposited particle side toward the substrate side, confirming that the scan traversed the Ti6Al4V/6061Al interface. Notably, on the particle side of the scan, a considerable Al signal was still detected despite the dominance of Ti, whereas on the substrate side, the Ti signal decreased significantly after crossing the interface but did not immediately drop to a negligible level, instead showing a gradual attenuation trend. These results indicate that interfacial bonding is not limited to physical contact and mechanical interlocking, but is also accompanied by limited elemental migration and compositional gradation.[57,58]

4.3. Mechanistic significance of solid-state deposition for "limited mutual solubility heterogeneous metals"

In the Al/Ti "limited mutual solubility heterogeneous metal" system, the core contradiction of interfacial connection lies in the trade-off between heat and integrity: increasing heat input aids interfacial wetting and bonding but significantly raises the risk of forming brittle Al/Ti intermetallic compound layers and thermal damage. Conversely, reducing heat input avoids reaction embrittlement but easily leads to interfacial porosity and weak bonding due to insufficient plastic flow. Therefore, a more feasible path for this system is to achieve effective bonding through solid-state impact-induced interfacial plastic flow and surface cleaning while avoiding the

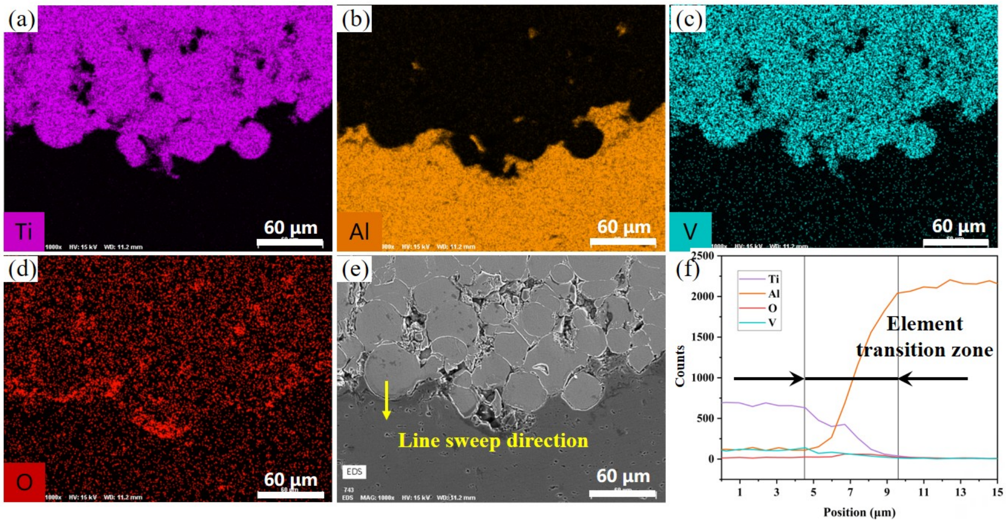

Figure 14. Scanning electron microscopy–energy-dispersive spectrometry maps (a–e) and line-scan results (f) across the Ti6Al4V/6061Al interface in the laser-assisted cold spray (LACS)-600 W sample. Scale bars: 60 μm; magnifications: 1,000×.

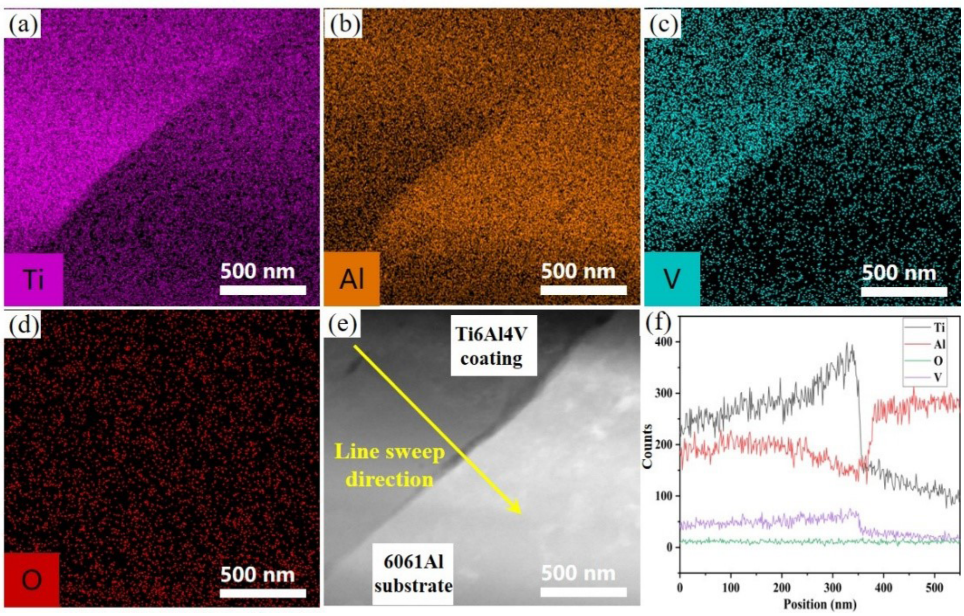

Figure 15. Transmission electron microscopy–energy-dispersive spectroscopy (TEM–EDS) elemental maps (a–e) and line-scan results (f) of the Ti6Al4V/6061Al interface in the laser-assisted cold spray (LACS)-600 W sample. Scale bars: 500 nm; magnifications: 48,000×.

melting–resolidification process.

The XRD results of this study showed that the diffraction peaks of samples from all process conditions remained consistent with the original Ti6Al4V powder. No obvious new phase peaks were detected, confirming the absence of detectable brittle Al/Ti compound peaks within the resolution limits of XRD. From the perspective of phase composition, this indicates that within the laser power window of this study, the laser primarily serves as a thermal-activation/flow-stress-reduction aid. The deposition process as a whole remains in the deposition domain dominated by solid-state impact plastic deformation and has not transformed into a large-scale fusion metallurgical reaction path. For limited mutual solubility between heterogeneous metals, this carries significant mechanistic meaning: solid-state deposition can achieve densification and performance improvements while minimizing the inherent risks of high-temperature paths, such as reaction-layer embrittlement, residual-stress concentration, and interfacial reliability degradation.

Meanwhile, combined with the aforementioned SEM/porosity and EBSD results, it is clear that laser assistance does not enhance bonding through a liquid-phase reaction layer. Instead, it improves deposition quality by promoting particle flattening, pore closure, and microstructural homogenization. Thus, the advantage of LACS in the Al/Ti limited mutual solubility system can be summarized as strengthening the impact of plastic flow and defect evolution (recovery/recrystallization) through moderate heat input while maintaining solid-state deposition characteristics and phase stability, achieving higher density and a more stable strength–ductility match. This mechanistic framework provides a more tolerant and reliable process route for heterogeneous metal additive manufacturing: replacing "high-temperature melting + reaction layer connection" with "low thermal influence + intense plastic flow," making it more suitable for Al/Ti composite/connection scenarios sensitive to brittle intermetallics.

5. Conclusion

This study conducted an in-depth exploration of the microstructural evolution and bonding mechanism of LACS-deposited Ti6Al4V on 6061Al substrates. The conclusions are as follows:

(i) Within the 0–800 W laser power range, the deposition process consistently maintained solid-state characteristics. XRD detected no β phase or brittle Al/Ti intermetallic peaks within its detection limits, suggesting that the embrittlement risks common in heterogeneous metal joining were minimized under the current characterization scale.
(ii) The coating exhibits typical longitudinal stratification, with laser-assisted densification having the greatest effect on the middle deposition layer. Under the 600 W condition, the porosity dropped to 0.41%, particle flattening was most significant, and the pore-closure mechanism shifted from mechanical stacking to intense plastic flow induced by thermo-mechanical coupling.
(iii) EBSD analysis showed that the LACS-600 W coating grains were refined from 1.906 μm to 0.813 μm, and the dynamic recrystallization proportion significantly increased from 18.05% to 38.35%. TEM characterization further confirmed a strain-gradient effect at the interface: particle edges adjacent to the interface formed randomly oriented nanocrystals due to extremely high shear strain, while the degree of refinement decreased with strain attenuation in regions farther from the interface.
(iv) The SEM–EDS and TEM–EDS results show that a ~5 μm elemental transition zone formed at the Ti6Al4V/6061Al interface under the LACS-600 W condition, with Ti and Al exhibiting continuous compositional variation across the interface. The results suggest localized elemental redistribution near the interface, although the contribution of atomic-scale diffusion requires further verification by higher-resolution characterization techniques.
(v) As laser power increased, the coating microhardness rose in steps, reaching a maximum of 388.1 $HV_{0.2}$. In LACS-600 W samples, the safety margin for interface failure significantly improved; all pull-off tests resulted in adhesive-layer failure, indicating that the true interfacial bonding strength has exceeded the limit of the adhesive.
(vi) Regarding tensile properties, the strength and ductility of the LACS-600 W coating achieved a substantial synergistic enhancement. The performance levels approached the lower-bound indices of samples produced via helium carrier gas CS or those subjected to specific post-deposition thermal treatments. While significantly reducing operational costs, the nitrogen-based LACS process provides a highly reliable solid-state additive manufacturing solution for the fabrication of high-performance Ti6Al4V/6061Al heterogeneous metal composite structures.

Acknowledgments

None.

Funding

This work was supported by the National Key Research and Development Program of China (Grant No. 2024YFB4609600); "Pioneer" and "Leading Goose" Research and Development Program of Zhejiang Province (2026C02A1211); Zhejiang Provincial Natural Science Foundation of China (LQN25E050015); Young Talent Project of GDAS (2025GDASQNRC-0304); and GDAS Project of Science and Technology Development (2024GDASZH-2024010102).

Conflict of interest

The authors declare that they have no known competing financial interests or personal relationships that could have appeared to influence the work reported in this paper.

Author contributions

Conceptualization: Shaowu Liu, Jianhua Yao
Data curation: Shaowu Liu

Formal analysis: Hongjian Wu
Funding acquisition: Shaowu Liu
Investigation: Shen Wang, Yehao Zhang
Methodology: Wenbo Li
Resources: Wenbo Li
Software: Shen Wang, Yehao Zhang
Supervision: Bo Li
Validation: Bo Li, Panpan Zhang
Visualization: Shen Wang
Writing–original draft: Shaowu Liu, Shen Wang
Writing–review & editing: Hongjian Wu, Zexin Yu, Shuo Yin, Qunli Zhang, Hanlin Liao, Jianhua Yao

Ethics approval and consent to participate

Not applicable.

Consent for publication

Not applicable.

Availability of data

The data used in this work are available upon reasonable request to the corresponding author.

References

1. Williams JC, Starke EA. Progress in structural materials for aerospace systems. *Acta Mater.* 2003;51(19):5775-5799.

   doi: 10.1016/j.actamat.2003.08.023

2. Xu Z, Ouyang W, Liu Y, Jiao J, Liu Y, Zhang W. Effects of laser polishing on surface morphology and mechanical properties of additive manufactured TiAl components. *J Manuf Process.* 2021;65:51-59.

   doi: 10.1016/j.jmapro.2021.03.014

3. Li SS, Yue X, Li QY, *et al.* Development and applications of aluminum alloys for aerospace industry. *J Mater Res Technol.* 2023;27:944-983.

   doi: 10.1016/j.jmrt.2023.09.274

4. Cao M, Wang CJ, Deng KK, Nie KB, Liang W, Wu YC. Effect of interface on mechanical properties and formability of Ti/Al/Ti laminated composites. *J Mater Res Technol.* 2021;14:1655-1669.

   doi: 10.1016/j.jmrt.2021.07.021

5. Que B, Chen L, Qian L, Kong X, Zhao G. Tailoring the microstructure of Al/Ti laminated composite through hot press sintering process to achieve superior mechanical properties. *J Mater Process Technol.* 2024;326:118349.

   doi: 10.1016/j.jmatprotec.2024.118349

6. Fang Z-C, Wu Z-L, Huang C-G, Wu C-W. Review on residual stress in selective laser melting additive manufacturing of alloy parts. *Opt Laser Technol.* 2020;129:106283.

   doi: 10.1016/j.optlastec.2020.106283

7. Li Z, Chai L, Qi L, *et al.* Laser-cladded Al-Cr-Ti ternary alloy coatings on Ti-4Al-2V alloy: Specific microstructure and enhanced surface performance. *Surf Coat Technol.* 2023;452:129073.

   doi: 10.1016/j.surfcoat.2022.129073

8. Yin S, Yan X, Chen C, Jenkins R, Liu M, Lupoi R. Hybrid additive manufacturing of Al-Ti6Al4V functionally graded materials with selective laser melting and cold spraying. *J Mater Process Technol.* 2018;255:650-655.

   doi: 10.1016/j.jmatprotec.2018.01.015

9. Zhang J, Wang X, Gao J, *et al.* Additive manufacturing of Ti–6Al–4V/Al–Cu–Mg multi-material structures with a Cu interlayer. *Int J Mech Sci.* 2023;256:108477.

   doi: 10.1016/j.ijmecsci.2023.108477

10. Chen X, Lei Z, Chen Y, *et al.* Microstructure and tensile properties of Ti/Al dissimilar joint by laser welding-brazing at subatmospheric pressure. *J Manuf Process.* 2020;56:19-27.

    doi: 10.1016/j.jmapro.2020.04.062

11. Moridi A, Hassani-Gangaraj SM, Guagliano M, Dao M. Cold spray coating: review of material systems and future perspectives. *Surf Eng.* 2014;30(6):369-395.

    doi: 10.1179/1743294414Y.0000000270

12. Raoelison RN, Xie Y, Sapanathan T, *et al.* Cold gas dynamic spray technology: A comprehensive review of processing conditions for various technological developments till to date. *Addit Manuf.* 2018;19:134-159.

    doi: 10.1016/j.addma.2017.07.001

13. Rokni M, Nutt S, Widener C, Champagne V, Hrabe R. Review of relationship between particle deformation, coating microstructure, and properties in high-pressure cold spray. *J Therm Spray Technol.* 2017;26(6):1308-1355.

    doi: 10.1007/s11666-017-0575-0

14. Lett S, Cormier J, Quet A, Villechaise P, Meillot E, Hémery S. Microstructure optimization of cold sprayed Ti-6Al-4V using post-process heat treatment for improved mechanical properties. *Addit Manuf.* 2024;86:104168.

    doi: 10.1016/j.addma.2024.104168

15. Wang Q, Han P, Yin S, *et al.* Current research status on cold sprayed amorphous alloy coatings: A review. *Coatings.* 2021;11(2):206.

    doi: 10.3390/coatings11020206

16. Yin S, Chen C, Suo X, Lupoi R. Cold-Sprayed Metal Coatings with Nanostructure. *Adv Mater Sci Eng.* 2018;2018(1):2804576.

    doi: 10.1155/2018/2804576

17. Bae G, Kumar S, Yoon S, *et al.* Bonding features and associated mechanisms in kinetic sprayed titanium

coatings. *Acta Mater.* 2009;57(19):5654-5666.

doi: 10.1016/j.actamat.2009.07.061

18. Li WY, Cao CC, Yin S. Solid-state cold spraying of Ti and its alloys: A literature review. *Prog Mater Sci.* 2020;110:100633.

    doi: 10.1016/j.pmatsci.2019.100633

19. Wei J, Aghasibeig M, Lyu T, *et al.* Cold spray deposition and microstructure characterization of CuNi, CuSn, and CuNiSiCr coatings. *Surf Coat Technol.* 2024;480:130621.

    doi: 10.1016/j.surfcoat.2024.130621

20. Yin S, Wang X, Suo X, *et al.* Deposition behavior of thermally softened copper particles in cold spraying. *Acta Mater.* 2013;61(14):5105-5118.

    doi: 10.1016/j.actamat.2013.04.041

21. Xie XL, Yin S, Raoelison RN, *et al.* Al matrix composites fabricated by solid-state cold spray deposition: A critical review. *J Mater Sci Technol.* 2021;86:20-55.

    doi: 10.1016/j.jmst.2021.01.026

22. Wei Y-K, Luo X-T, Chu X, Huang G-S, Li C-J. Solid-state additive manufacturing high performance aluminum alloy 6061 enabled by an in-situ micro-forging assisted cold spray. *Mater Sci Eng A.* 2020;776:139024.

    doi: 10.1016/j.msea.2020.139024

23. Kovarik O, Cizek J, Yin S, *et al.* Mechanical and Fatigue Properties of Diamond-Reinforced Cu and Al Metal Matrix Composites Prepared by Cold Spray. *J Therm Spray Technol.* 2022;31(1-2):217-233.

    doi: 10.1007/s11666-022-01321-3

24. Dai S, Cui MC, Li JH, Zhang M. Cold Spray Technology and Its Application in the Manufacturing of Metal Matrix Composite Materials with Carbon-Based Reinforcements. *Coatings.* 2024;14(7):822.

    doi: 10.3390/coatings14070822

25. Zórawski W, Molak R, Madry J, *et al.* Experimental and Numerical Investigations of Titanium Deposition for Cold Spray Additive Manufacturing as a Function of Standoff Distance. *Materials.* 2021;14(19):5492.

    doi: 10.3390/ma14195492

26. Drehmann R, Colditz P, Graf M, *et al.* Forming Behavior of Additively Manufactured Al/Ti Material Compounds Produced by Cold Spraying. *J Therm Spray Technol.* 2024;33(2):676-687.

    doi: 10.1007/s11666-023-01699-8

27. Shen L, Kong LY, Xiong TY, Du H, Li TF. Preparation of TiAl3-Al composite coating by cold spraying. *Trans Nonferrous Met Soc China.* 2009;19(4):879-882.

    doi: 10.1016/S1003-6326(08)60369-6

28. Bray M, Cockburn A, O'Neill W. The Laser-assisted Cold Spray process and deposit characterisation. *Surf Coat Technol.* 2009;203(19):2851-2857.

    doi: 10.1016/j.surfcoat.2009.02.135

29. Olakanmi EO, Doyoyo M. Laser-Assisted Cold-Sprayed Corrosion- and Wear-Resistant Coatings: A Review. *J Therm Spray Technol.* 2014;23(5):765-785.

    doi: 10.1007/s11666-014-0098-x

30. Wang K, Zhao L, Mao T, Cui X, Wang J, Xiong T. Effect of laser power on the microstructure and mechanical properties of laser-assisted cold sprayed 7075 aluminum alloy deposits. *Mater Sci Eng A.* 2023;879:145224.

    doi: 10.1016/j.msea.2023.145224

31. Qi Z, Li Y, Chu X, Xie Y, Long Y. Effect of laser power on microstructure and properties of laser assisted cold sprayed copper coatings on steel. *Surf Coat Technol.* 2024;477:130308.

    doi: 10.1016/j.surfcoat.2023.130308

32. Boese S, Sevinsky A, Nourian-Avval A, Özdemir O, Müftü S. Laser assisted cold spray of aluminum alloy 6061: Experimental results. *Addit Manuf.* 2024;95:104548.

    doi: 10.1016/j.addma.2024.104548

33. Yin S, Fan N, Huang C, *et al.* Towards high-strength cold spray additive manufactured metals: Methods, mechanisms, and properties. *J Mater Sci Technol.* 2024;170:47-64.

    doi: 10.1016/j.jmst.2023.05.047

34. Yao J, Yang L, Li B, Li Z. Beneficial effects of laser irradiation on the deposition process of diamond/Ni60 composite coating with cold spray. *Appl Surf Sci.* 2015;330:300-308.

    doi: 10.1016/j.apsusc.2015.01.029

35. Li B, Yao J, Zhang Q, Li Z, Yang L. Microstructure and tribological performance of tungsten carbide reinforced stainless steel composite coatings by supersonic laser deposition. *Surf Coat Technol.* 2015;275:58-68.

    doi: 10.1016/j.surfcoat.2015.05.040

36. Boruah D, McNutt P, Sharma D, Begg H, Zhang X. Understanding the Effect of Substrate Preheating Temperature and Track Spacing on Laser Assisted Cold Spraying of Ti6Al4V. *Metals.* 2023;13(10):1640.

    doi: 10.3390/met13101640

37. Birt AM, Champagne VK, Sisson RD, Apelian D. Statistically Guided Development of Laser-Assisted Cold Spray for Microstructural Control of Ti-6Al-4V. *Metall Mater Trans A.* 2017;48(4):1931-1943.

    doi: 10.1007/s11661-017-3970-8

38. Williamson GK, Hall WH. X-ray line broadening from filed aluminium and wolfram. *Acta Metall.* 1953;1(1):22-31.

    doi: 10.1016/0001-6160(53)90006-6

39. ASTM. *Standard Test Method for Adhesion or Cohesion*

Strength of Thermal Spray Coatings (ASTM 633-01). West Conshohocken, PA: ASTM International; 2008.

40. Jafari R, Honkanen M, Amer M, *et al*. Impact-induced deformation and microstructural evolution in cold-spray deposition of aluminum alloy–quasicrystal composite: A characterization perspective. *Mater Des.* 2025;253:113977.

    doi: 10.1016/j.matdes.2025.113977

41. Zhou HX, Jiang SW, Li XT, Li CX. Deposition behavior and bonding mechanism during cold spraying of Ti6Al4V on different substrates. *Surfaces Interfaces.* 2022;33:102237.

    doi: 10.1016/j.surfin.2022.102237

42. Gao J, Cao Y, Lu L, *et al*. Study on the interaction between nanosecond laser and 6061 aluminum alloy considering temperature dependence. *J Alloys Compd.* 2022;892:162044.

    doi: 10.1016/j.jallcom.2021.162044

43. Huang K, Logé RE. A review of dynamic recrystallization phenomena in metallic materials. *Mater Des.* 2016;111:548-574.

    doi: 10.1016/j.matdes.2016.09.012

44. Allain-Bonasso N, Wagner F, Berbenni S, Field DP. A study of the heterogeneity of plastic deformation in IF steel by EBSD. *Mater Sci Eng A.* 2012;548:56-63.

    doi: 10.1016/j.msea.2012.03.068

45. Schwartz AJ, Kumar M, Adams BL, Field DP. *Electron Backscatter Diffraction in Materials Science*. Vol 2. New York, NY: Springer; 2009.

46. Cordero ZC, Knight BE, Schuh CA. Six decades of the Hall–Petch effect – a survey of grain-size strengthening studies on pure metals. *Int Mater Rev.* 2016;61(8):495-512.

    doi: 10.1080/09506608.2016.1191808

47. Hansen N. Hall–Petch relation and boundary strengthening. *Scr Mater.* 2004;51(8):801-806.

    doi: 10.1016/j.scriptamat.2004.06.002

48. Chen C, Xie Y, Yan X, *et al*. Effect of hot isostatic pressing (HIP) on microstructure and mechanical properties of Ti6Al4V alloy fabricated by cold spray additive manufacturing. *Addit Manuf.* 2019;27:595-605.

    doi: 10.1016/j.addma.2019.03.028

49. Petrovskiy P, Travyanov A, Cheverikin VV, Chereshneva AA, Sova A, Smurov I. Effect of encapsulated hot isostatic pressing on properties of Ti6Al4V deposits produced by cold spray. *Int J Adv Manuf Technol.* 2020;107(1):437-449.

    doi: 10.1007/s00170-020-05080-9

50. Petrovskiy P, Khomutov M, Cheverikin V, Travyanov A, Sova A, Smurov I. Influence of hot isostatic pressing on the properties of 316L stainless steel, Al-Mg-Sc-Zr alloy, titanium and Ti6Al4V cold spray deposits. *Surf Coat Technol.* 2021;405:126736.

    doi: 10.1016/j.surfcoat.2020.126736

51. Ligda JP, Butler BG, Saenz N, Paramore J. Mechanical Behavior of Additively Manufactured Ti-6Al-4V Following a New Heat Treatment. In: Kramer S, Jordan J, Jin H, Carroll J, Beese A, eds. *Mechanics of Additive and Advanced Manufacturing, Volume 8*. Conference Proceedings of the Society for Experimental Mechanics Series. Cham, Switzerland: Springer International Publishing; 2019:29-30.

    doi: 10.1007/978-3-319-95083-9_6

52. Boruah D, Zhang X, McNutt P, Khan R, Begg H. Effect of Post-Deposition Thermal Treatments on Tensile Properties of Cold Sprayed Ti6Al4V. *Metals.* 2022;12(11):1908.

    doi: 10.3390/met12111908

53. Arabgol Z, Villa Vidaller M, Assadi H, Gärtner F, Klassen T. Influence of thermal properties and temperature of substrate on the quality of cold-sprayed deposits. *Acta Mater.* 2017;127:287-301.

    doi: 10.1016/j.actamat.2017.01.040

54. Singh S, Raman RKS, Berndt CC, Singh H. Influence of Cold Spray Parameters on Bonding Mechanisms: A Review. *Metals.* 2021;11(12):2016.

    doi: 10.3390/met11122016

55. Yang L, Wang P, Luo X, *et al*. Nanocrystallization of interfacial microstructure of deformed particles in cold sprayed Ti6Al4V deposits. *Mater Des.* 2021;210:110117.

    doi: 10.1016/j.matdes.2021.110117

56. Liu S, Zheng W, Wang S, *et al*. Synergistic optimization of heterogeneous interface bonding and surface performance of 316 stainless steel coatings deposited on 7050Al alloy substrates via laser-assisted cold spray. *J Mater Res Technol.* 2026;43:225-240.

    doi: 10.1016/j.jmrt.2026.06.072

57. Li B, Cheng J, Wang H, *et al*. Improved inter-particle bonding of cold sprayed Ti6Al4V coatings by synchronously coupling with laser irradiation and in-situ shot peening during deposition process. *Surf Coat Technol.* 2026;533:133654.

    doi: 10.1016/j.surfcoat.2026.133654

58. Ding XY, Fu YC, Li B, *et al*. Microstructure and mechanical properties of Al2O3 dispersion strengthened Cu by laser in-situ aluminum thermal reduction processing. *Mater Des.* 2025;258:114547.

    doi: 10.1016/j.matdes.2025.114547